

A full-chain simulation model for electron-bombarded active pixel sensors in low-light imaging

Zhen-Yuan Zhu(朱振源), Jing-Zhi Zhang(张景智), Yun-Sheng Qian(钱芸生), Yi-Jun Zhang(张益军), Yi-Lun Wang(王逸伦), and Gang-Cheng Jiao(焦岗成)

Citation: Chin. Phys. B, 2026, 35 (**8**): 084208. DOI: 10.1088/1674-1056/ae1725
http://cpb.iphy.ac.cn; http://iopscience.iop.org/cpb

What follows is a list of articles you may be interested in

Planar structure of organic photodetector for low dark current

Mohammad Nofil, Amirul Ashraf Md Sabri, Fadlan Arif Natashah, Tahani M Bawazeer, Mohammad S Alsoufi, Nur Adilah Roslan, and Azzuliani Supangat

Chin. Phys. B, 2025, 34 (**2**): 024204. DOI: 10.1088/1674-1056/ad9731

Analysis of relative wavelength response characterization and its effects on scanned-WMS gas sensing

Dao Zheng(郑道), Zhi-Min Peng(彭志敏), Yan-Jun Ding(丁艳军), and Yan-Jun Du(杜艳君)

Chin. Phys. B, 2021, 30 (**4**): 044210. DOI: 10.1088/1674-1056/abdb1c

Error analysis and Stokes parameter measurement of rotating quarter-wave plate polarimeter

Dan-Dan Zhi(支丹丹), Jian-Jun Li(李健军), Dong-Yang Gao(高冬阳), Wen-Chao Zhai(翟文超), Xiong-Hao Huang(黄雄豪), Xiao-Bing Zheng(郑小兵)

Chin. Phys. B, 2017, 26 (**12**): 124201. DOI: 10.1088/1674-1056/26/12/124201

Asymmetrical plasmon reflections in tapered graphene ribbons with wrinkle edges

Cui Yang(杨翠), Runkun Chen(陈闰堃), Yuping Jia(贾玉萍), Liwei Guo(郭丽伟), Jianing Chen(陈佳宁)

Chin. Phys. B, 2017, 26 (**7**): 074220. DOI: 10.1088/1674-1056/26/7/074220

UV–visible spectral characterization and density functional theory simulation analysis on laser-induced crystallization of amorphous silicon thin films

Huang Lu (黄璐), Jin Jing (金晶), Shi Wei-Min (史伟民), Yuan Zhi-Jun (袁志军), Yang Wei-Guang (杨伟光), Cao Ze-Chun (曹泽淳), Wang Lin-Jun (王林军), Zhou Jun (周军), Lou Qi-Hong (楼祺洪)

Chin. Phys. B, 2014, 23 (**3**): 034208. DOI: 10.1088/1674-1056/23/3/034208

A full-chain simulation model for electron-bombarded active pixel sensors in low-light imaging

Zhen-Yuan Zhu(朱振源)[1], Jing-Zhi Zhang(张景智)[1], Yun-Sheng Qian(钱芸生)[1,†], Yi-Jun Zhang(张益军)[1], Yi-Lun Wang(王逸伦)[1], and Gang-Cheng Jiao(焦岗成)[2]

[1] *School of Electronic and Optical Engineering, Nanjing University of Science and Technology, Nanjing* 210094, *China*
[2] *Science and Technology on Low-Light Level Night Vision Laboratory, Xi'an* 710065, *China*

(Received 31 July 2025; revised manuscript received 22 October 2025; accepted manuscript online 24 October 2025)

Electron-bombarded active pixel sensors (EBAPSs) have been widely used in low-light level night vision owing to their low-noise imaging performances under extremely low illumination. However, theoretical models of EBAPSs remain limited, resulting in insufficient prediction of their imaging performance. This study proposes a photon-to-gray conversion model that describes the full signal chain from optical input to digital output. A parameter calibration method was introduced, and the model was verified by comparing simulated images with experimental results obtained from a custom-developed EBAPS imager in an illumination-controlled dark lab. The comparison indicates that the average relative deviation in signal-to-noise ratio between simulation and experiment is within 10%. Furthermore, the simulated and experimental images exhibit consistent trends in limiting resolution with varying illumination. The validated model was further employed to investigate the influence of critical parameters on both SNR and resolution. This study establishes a reliable model that can complement or replace illumination-controlled dark lab testing in the performance evaluation of EBAPS imagers.

Keywords: low-light level (LLL) imaging, electron-bombarded active pixel sensor (EBAPS), photon-to-gray conversion, simulation analysis

PACS: 42.79.Pw, 42.79.Ls, 85.60.Ha, 85.60.–q

DOI: 10.1088/1674-1056/ae1725 **CSTR:** 32038.14.CPB.ae1725

1. Introduction

Low-light level (LLL) imaging technology employs LLL devices to capture images in extremely dark environments by leveraging the target's reflectance characteristics, which has demonstrated extensive applications across various domains including defense, high-energy physics, fluorescence microscopy, and aerospace.[1–5] In the early stages of LLL imaging technology, vacuum devices such as image intensifiers and camera tubes dominated the field owing to their high gain and low dark current.[6] With the progress of solid-state devices like CCD and CMOS sensors, digital imaging evolved rapidly. To integrate the high gain of vacuum devices with the digital advantages of solid-state technology, vacuum-solid hybrid devices have been developed and attracted increasing attention.[7,8] As a hybrid device, the electron-bombarded active pixel sensor (EBAPS) exhibits application prospects in LLL night vision owing to its capability to image under illumination conditions below 10^{-5} lx, high sensitivity, low noise, low power consumption, and digital image output.[9] Nevertheless, the EBAPS is confronted with inherent challenges stemming from its complex structure, high fabrication cost, and prolonged development cycle. Consequently, simulation-based design and performance prediction have become essential for EBAPS development.

In general, the image quality of solid devices is limited by multiple noise sources.[10–12] As a result, noise analysis and modeling are effective methods for predicting performance of imaging devices. Significant advancements have been achieved in noise modeling for solid-state image sensors. Zhang *et al.* modeled random telegraph signal noise in CMOS image sensors (CIS) under low-light conditions, revealing its long-tailed distribution and impact on sensitivity.[13] Wei *et al.* proposed a low-light CIS noise model that is applicable across different devices.[14] Bu *et al.* formulated a comprehensive noise analysis model encompassing the entire imaging chain of CCD sensors.[15] These studies provide valuable references for simulating noise behaviors in EBAPS. Nevertheless, EBAPS is a vacuum-solid hybrid sensor, so these noise models for solid-state image sensors cannot be applied to it directly.

In recent years, extensive research has been conducted on EBAPS modeling. Raner *et al.* developed a performance model for EBAPS, incorporating critical device parameters such as photocathode quantum efficiency (QE) and acceleration voltage as key variables.[16] However, the study was limited to single-photon detection scenarios and lacked experimental validation. In 2016, Hirvonen *et al.* linked photon arrival timing to electron-bombarded semiconductor (EBS)

†Corresponding author. E-mail: yunshengqiannjust@163.com

© 2026 Chinese Physical Society and IOP Publishing Ltd. All rights, including for text and data mining, AI training, and similar technologies, are reserved.

gain by using the pulse-height distribution of photon events, which varies with acceleration voltage.[17] In 2020, Wang *et al*. simulated the electrostatic field distribution of EBAPS and proposed a design of highly doped multiplication layer to optimize electron focusing.[18] In 2022, Wang *et al*. modeled the scattering behavior of incident photoelectrons on the back-side bombarded CMOS surface, quantitatively characterized the backscattered electrons (BSE), and their influence on resolution of EBAPS.[19] In 2024, Chen *et al*. theoretically established a universal gain model of the multiplying layer in EBAPS by considering elastic and inelastic scattering.[20] These existing studies have tended to research individual physical processes within the EBAPS imaging chain. A comprehensive photon-to-gray conversion model needs to be established for EBAPS imagers. Since noise is one of the important factors influencing the performance of imaging systems,[21] the model should consider the interactions among multiple noise sources.

This paper introduces a full-chain imaging simulation model for EBAPS imagers, covering critical processes such as illuminance attenuation, photoelectric conversion, electron multiplication, charge collection, and digital signal output. A parameter calibration method was introduced, and the effectiveness of the proposed model was verified by comparing simulated and experimentally captured images in an illumination-controlled dark lab. Finally, the validated model was employed to simulate and analyze the impact of key parameters, including dark noise and proximity-focusing distance, on the imaging performance of EBAPS imagers.

2. Photon-to-gray conversion model

The EBAPS comprises an entrance window, a transmission-type photocathode, and an electron-sensitive APS anode. Its internal structure is maintained under a high-vacuum environment and typically employs a proximity-focusing configuration, in which the distance between the photocathode and the APS defines the proximity-focusing distance d. As illustrated in Fig. 1, low light signals pass through the entrance window and strike the photocathode, which in turn emits photoelectrons. Accelerated by the high-voltage electric field $\boldsymbol{E}$ across the inter-electrode gap, the photoelectrons bombard the electron-sensitive APS anode, where they trigger electron multiplication.[22] In particular, the APS receives electrons rather than photons, and therefore does not incorporate microlenses as used in conventional CIS. These multiplied electrons are converted by the APS circuitry into voltage signals, which are then amplified and digitized by an analog-to-digital converter. The resulting digital values are finally mapped to gray levels for each pixel in the output image.

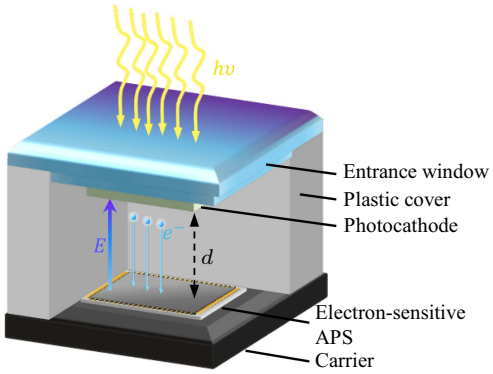


Fig. 1. Operating principle of EBAPS.

Given that EBAPS exhibits a linear response similar to CIS under a constant acceleration voltage, we developed a comprehensive mathematical model of its imaging chain. The imaging process was modeled under illumination-controlled dark lab conditions. Consequently, uncertain environmental factors such as weather conditions and target characteristics were fixed. The model is valid under three assumptions. First, the target is treated as an extended source coaxially aligned with the optical axis of the imager. Second, the target surface is approximated as a Lambertian, so its reflection follows the Lambert's cosine law. Third, the distance between the target and the imager is less than 5 m, so atmospheric attenuation of illuminance can be neglected. Under these conditions, the illuminance on the photocathode surface can be expressed as[23]

$$E_1 = \frac{E_0 \rho \tau}{4(f/\#)^2 + 1}, \tag{1}$$

where E_0 denotes the ambient illuminance (lx), ρ represents the reflectance of the target, τ is the average transmittance of the lens, and $f/\#$ is the f-number.

Since the signal conversion mechanism is identical at each pixel of the EBAPS imager, the imaging process is modeled using the sensitive area of a single, arbitrarily chosen pixel on the APS surface. This region serves as the observation window and possesses a one-to-one projection onto the photocathode in the proximity-focused configuration. All subsequent signal conversion chains are analyzed within this window. The photon-to-gray conversion model based on the imaging chain of the EBAPS imager is shown in Fig. 2. Throughout the signal chain, each gain or transformation stage introduces signal-dependent noise. These fluctuations are characterized by the variance of the photon or electron count distribution, enabling a quantitative analysis of noise at each stage of the imaging process. The same approach is equally applicable to signal-independent noise sources. For this analysis, the mathematical relationship between the following statistical variables is introduced. When a statistical variable X is defined as the sum of the occurrences of a second variable Y with average y and variance σ_Y^2, and the number of occurrences is determined by a third statistical variable N with average n and variance

σ_N^2, the average x and variance σ_X^2 of X are given by[24]

$$X_i = \sum_k^{N_i} Y_k, \quad \begin{cases} x = ny, \\ \sigma_X^2 = n\sigma_Y^2 + y^2\sigma_N^2. \end{cases} \tag{2}$$

After modeling the illuminance attenuation, the mean number of photons n_{p} (photons/frame·pixel) received on the photocathode surface can be expressed as

$$n_{\mathrm{p}} = \phi_{\mathrm{px}} T_{\mathrm{exp}} \sum_{\lambda_1}^{\lambda_2} N_{\mathrm{ph}}(\lambda) \cdot \Delta\lambda, \tag{3}$$

where T_{exp} is the exposure time, and $N_{\mathrm{ph}}(\lambda)$ represents the photon distribution corresponding to 1 lm of photon flux within the EBAPS spectral response range $[\lambda_1, \lambda_2]$. $\Delta\lambda$ is the sampling step in wavelength determined by the QE curve. ϕ_{px} (lm pixel) represents the average photon flux received on the photocathode surface. It can be calculated as $\phi_{\mathrm{px}} = ES_{\mathrm{px}}$, where S_{px} is the area of sensitive region of a single pixel in $\mu\mathrm{m}^2$. The number of photons incident in a given observation window is known to follow a Poisson distribution.[25] Therefore, the incident photons can be described as $N_{\mathrm{p}} \sim P(n_{\mathrm{p}})$, where $P(\cdot)$ denotes the Poisson distribution. In addition, the random fluctuations caused by incident photons are expressed as photon shot noise σ_{p}.

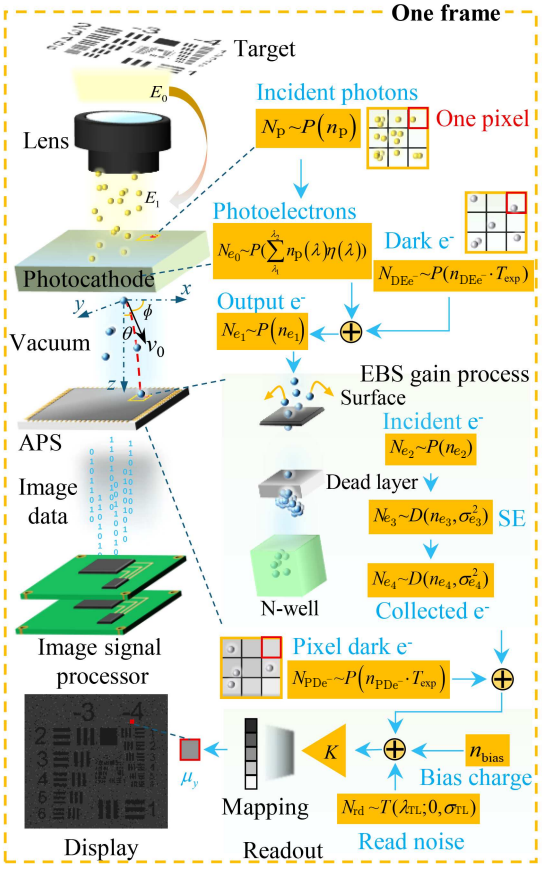


Fig. 2. Photon-to-gray conversion model.

Photon conversion at wavelength λ is modeled as an independent Bernoulli trial with a success probability equal to the photocathode QE $\eta(\lambda)$. For incident photons $N_{\mathrm{p}}(\lambda)$, the number of photoelectrons $N_{e_0}(\lambda)$ follows a compound Poisson distribution: $N_{e_0}(\lambda) = \sum_1^{N_{\mathrm{p}}(\lambda)} \eta_j(\lambda)$, where $\eta_j(\lambda)$ denotes the probability of the j-th photon being converted into a photoelectron. The total number of photoelectrons generated over the entire spectral response range $[\lambda_1, \lambda_2]$ follows the Poisson distribution:

$$N_{e_0} \sim P\left(\sum_{\lambda_1}^{\lambda_2} n_{\mathrm{p}}(\lambda)\eta(\lambda)\right). \tag{4}$$

Here, $n_{\mathrm{p}}(\lambda) = \phi_{\mathrm{px}} T_{\mathrm{exp}} N_{\mathrm{ph}}(\lambda) \cdot \Delta\lambda$ represents the mean number of photons received on a pixel. After photoelectric conversion, the total number of output electrons N_{e_1} is given by

$$N_{e_1} = N_{e_0} + N_{\mathrm{DEe^-}} \sim P(n_{e_1}). \tag{5}$$

In Eq. (5), $N_{\mathrm{DEe^-}}$ represents the number of dark electrons emitted by the photocathode during the exposure time, expressed as $N_{\mathrm{DEe^-}} \sim P\left(n_{\mathrm{DEe^-}} \cdot T_{\mathrm{exp}}\right)$, where $n_{\mathrm{DEe^-}}$ is the dark emission rate of the photocathode. The average n_{e_1} is the sum of the expectations of the two statistically independent Poisson distributions representing photoelectrons and dark emission electrons.

As shown in Fig. 2, the trajectories of these electrons in vacuum are parabolic, and their lateral displacement at the silicon–vacuum interface is given by

$$\begin{cases} \Delta x(\varepsilon, \theta, \phi) = v_0(\varepsilon) t_z(\varepsilon, \theta) \sin\theta \cos\phi, \\ \Delta y(\varepsilon, \theta, \phi) = v_0(\varepsilon) t_z(\varepsilon, \theta) \sin\theta \sin\phi. \end{cases} \tag{6}$$

Here, $v_0(\varepsilon) = (2e\varepsilon E_{\mathrm{max}}/m_{\mathrm{e}})^{1/2}$ represents the initial velocity magnitude, where e represents the charge of an electron and m_{e} represents the electron mass. The normalized emission energy ε is modeled by a Beta distribution Beta (α, β) with parameters $\alpha = 1, \beta = 8$.[26] $E_{\mathrm{max}} = hc(1/\lambda_1 - 1/\lambda_2)$ is the maximum initial emission energy within the photocathode's spectral response range $[\lambda_1, \lambda_2]$, where h denotes Planck's constant and c represents the speed of light. The initial emission angle θ follows the Lambert's cosine law,[26] while the azimuthal angle ϕ follows a uniform distribution. The transit time across the vacuum can be expressed by

$$t_z(\varepsilon, \theta) = \frac{-v_0(\varepsilon)\cos\theta + \sqrt{v_0^2(\varepsilon)\cos^2\theta + 2a_z d}}{a_z}, \tag{7}$$

where $a_z = eE/m_{\mathrm{e}}$ is the acceleration along the $+z$ direction. The electric field strength is given by $E = V_{\mathrm{aclr}}/d$.

To quantify the electron dispersion in proximity-focusing configuration, the sampled lateral displacements are converted into pixel coordinates, and the number of electrons at each pixel location is accumulated. The output distribution is then expressed as

$$Y[i, j] = \sum_{m,n} X[m, n] K[i - m, j - n], \tag{8}$$

where $X[m,n]$ denotes the number of electrons emitted from the photocathode at pixel (m,n) and K $[u,\ v]$ represents the probability that an electron emitted from the photocathode contributes to pixel $(u,\ v)$ on the silicon–vacuum interface and its surrounding pixels. In the ideal case, the kernel is normalized as $\sum_{m,n} K[u,v] = 1$. Based on Eq. (5), $X[m,n]$ follows a Poisson distribution, the output $Y[i,j]$ is also a Poisson random variable. Electron number conservation ensures that the total number of electrons at the silicon–vacuum interface remains equal to that emitted from the photocathode, denoted N_{e_1}. Moreover, this process does not alter the Poisson nature of the distribution, and thus the overall expectation and variance are preserved.

Subsequently, the EBS gain process begins, as illustrated in Fig. 2. Some high-energy electrons undergo one or multiple scattering events, deviating from their original trajectory and returning to the vacuum region.[19] Such electrons are termed BSE. Under the influence of the electric field between the photocathode and the electron-sensitive APS, BSE may re-enter the APS. However, because they retain only half of their initial energy after scattering, this re-entry is considered negligible.[27,28] Consequently, in the statistical modeling of the backscattering process, only the electrons that successfully enter the electron-sensitive APS are considered. The average proportion of BSE among incident electrons is described by the backscattering coefficient γ. This coefficient is positively correlated with the atomic number of the target material and negatively correlated with the acceleration voltage. In this model, the target material is silicon, so only the variation of the coefficient with acceleration voltage is considered. The data are sourced from the electron-solid interaction database established by Joy.[29] Whether each electron bombardment on the APS surface undergoes backscattering follows an independent and identically distributed Bernoulli process with an expectation of γ. Accordingly, the number of electrons entering the APS can be expressed as $N_{e_2} = \sum_1^{N_{e_1}} (1-\gamma_k)$, where γ_k denotes the backscattering probability of the k-th electron. Based on Eq. (2), N_{e_2} can be expressed as $N_{e_2} \sim P(n_{e_2})$, where $n_{e_2} = n_{e_1}(1-\gamma)$.

After passing through the silicon–vacuum surface, incident electrons collide with atoms in the dead layer. Each electron produces a random number of secondary electrons (SE) following a normal distribution with a mean of G_{EB} and a standard deviation of σ_{EB}.[16] Therefore, the total number of SE can be expressed as $N_{e_3} = \sum_1^{N_{e_2}} G_{\mathrm{EB}}^{(k)}$, where $G_{\mathrm{EB}}^{(k)}$ represents the EBS gain associated with the *k-th* primary electron. According to Eq. (2), the expectation n_{e_3} and variance $\sigma_{e_3}^2$ of N_{e_3} are given by

$$\begin{cases} n_{e_3} = n_{e_2} G_{\mathrm{EB}}, \\ \sigma_{e_3}^2 = n_{e_2}\sigma_{\mathrm{EB}}^2 + G_{\mathrm{EB}}^2\sigma_{e_2}^2 = \left(\sigma_{\mathrm{EB}}^2 + G_{\mathrm{EB}}^2\right) n_{e_2}. \end{cases} \tag{9}$$

In Eq. (9), the EBS gain G_{EB} is calculated by $G_{\mathrm{EB}} = (V_{\mathrm{aclr}} - V_{\mathrm{thr}})/W$, where V_{aclr} denotes the acceleration voltage, V_{thr} denotes the threshold voltage corresponding to the energy loss as the electron passes through the dead layer of the pixel entrance surface,[30] and W is the energy required to generate an electron–hole pair in the semiconductor. For silicon, W is 3.64 eV.[31] In this model, optimization of the entrance surface is assumed, so the energy loss could be ignored, $V_{\mathrm{thr}} = 0$. Due to the random distribution of discrete electron energy between bond breakage and lattice vibrations, the number of SE generated follows a probability distribution between Poisson and Dirac distributions. The statistical characteristics of the noise in this process are governed by the Fano factor F_{F}, which has a value of 0.119 for silicon.[32] Consequently, the variance of the electron multiplication process is given by $\sigma_{\mathrm{EB}}^2 = F_{\mathrm{F}} G_{\mathrm{EB}}$.[33] Since N_{e_3} does not follow any known standard probability distribution, it is expressed as $N_{e_3} \sim D(n_{e_3}, \sigma_{e_3}^2)$, where $D(\cdot)$ denotes an unspecified probability distribution with a given average and variance.

A significant portion of SE recombine within the dead layer. Electrons that successfully traverse this region diffuse along the concentration gradient toward the N-well of the photodiode in the electron-sensitive APS, where they are ultimately collected. The collection for each electron can be modeled as a Bernoulli trial, with the collection efficiency serving as the average success probability, which decreases with thicker passivation or multiplication layers, lower incident-electron energy, and smaller electrode size. According to Eq. (2), the statistical quantity of successfully collected electrons N_{e_4}, along with its average n_{e_4} and variance $\sigma_{e_4}^2$, are given by

$$\begin{aligned} &N_{e_4} = \sum_k^{N_{e_3}} CE^{(k)}, \\ &\begin{cases} n_{e_4} = n_{e_3} CE, \\ \sigma_{e_4}^2 = n_{e_3}\sigma_{CE}^2 + CE^2\sigma_{e_3}^2 = n_{e_3}(1-CE)CE + CE^2\sigma_{e_3}^2. \end{cases} \end{aligned} \tag{10}$$

Here, $CE^{(k)}$ represents the probability that the k-th secondary electron is collected. Since N_{e_4} does not follow any standard distribution, it can be expressed as $N_{e_4} \sim D(n_{e_4}, \sigma_{e_4}^2)$. Alongside charge collection, the pixel dark electrons also accumulate during the exposure, which follow a Poisson process. The corresponding statistical quantity can be expressed as $N_{\mathrm{PDe^-}} \sim P\left(n_{\mathrm{PDe^-}} \cdot T_{\mathrm{exp}}\right)$, where $n_{\mathrm{PDe^-}}$ denotes the pixel dark electrons accumulation rate. The total number of electrons N_{e} prior to readout comprises both the collected electrons and the pixel dark electrons, which are statistically independent random variables. Therefore, N_{e} can be derived as

$$N_{\mathrm{e}} \sim D\left(n_{e_4} + n_{\mathrm{PDe^-}} \cdot T_{\mathrm{exp}}, \sigma_{e_4}^2 + n_{\mathrm{PDe^-}} \cdot T_{\mathrm{exp}}\right). \tag{11}$$

In the logic circuitry of the electron-sensitive APS, the charge is converted into a voltage signal through a sensing ca-

pacitor. The voltage is then amplified and digitalized to generate gray values. During this process, read noise N_{rd} is introduced by the readout circuitry and the in-pixel amplifier. As this noise typically exhibits heavy-tailed characteristics,[14] it is modeled using the Tukey-lambda distribution: $N_{\mathrm{rd}} \sim T(\lambda_{\mathrm{TL}};\mu_{\mathrm{c}};\sigma_{\mathrm{TL}})$, where $T(\cdot)$ denotes the Tukey-lambda distribution. Here, λ_{TL} and σ_{TL} represent the shape and scale parameters, and μ_{c} denotes the direct current noise component. To prevent negative output values, a constant positive bias charge n_{bias} is added to each pixel before analog-to-digital conversion. Since the bias charge dominates the direct current component, μ_{c} is set to zero. To simulate the digital signal output, a conversion gain K is introduced, representing the gain from charge to grayscale. Therefore, the mean digital gray value μ_y (DN/frame pixel) and the total output noise σ_{total} (e^- rms) are given by

$$\begin{aligned}\mu_y &= Kn_{\mathrm{e}} = K\Bigg[\mathrm{CEG_{EB}}(1-\gamma)\Bigg(\sum_{\lambda_1}^{\lambda_2} n_{\mathrm{p}}(\lambda)\eta(\lambda) \\ &\quad + n_{\mathrm{DEe^-}}\cdot T_{\mathrm{exp}}\Bigg) + n_{\mathrm{PDe^-}}\cdot T_{\mathrm{exp}} + n_{\mathrm{bias}}\Bigg], \\ \sigma_{\mathrm{total}} &= \left(\sigma_{\mathrm{e}}^2+\sigma_{\mathrm{TL}}^2\right)^{1/2} = \Bigg(\Bigg(\sum_{\lambda_1}^{\lambda_2} n_{\mathrm{p}}(\lambda)\eta(\lambda) + n_{\mathrm{DEe^-}}\Bigg) \\ &\quad \times (1-\gamma)G_{\mathrm{EB}}CE\left[1-CE+CE\left(F_{\mathrm{F}}+G_{\mathrm{EB}}\right)\right] \\ &\quad + n_{\mathrm{PDe^-}}\cdot T_{\mathrm{exp}} + \sigma_{\mathrm{TL}}^2\Bigg)^{1/2}. \end{aligned} \tag{12}$$

3. Calibration of parameters in the photon-to-gray conversion model

Based on Eq. (12), the imaging simulation of EBAPS imagers can be performed by using a target input image. In practical applications, it is essential to calibrate the model parameters so that simulated images closely match the captured ones. This calibration process was conducted in an illumination-controlled dark lab, focusing on the following variables: photocathode QE, conversion gain, pixel dark electrons, collection efficiency, bias charge, photocathode dark emission electrons, and read noise. The experimental setup for parameter calibration is shown in Fig. 3. We used a custom-developed EBAPS device comprising a GaAs photocathode and a backside-illuminated CIS with a 9.7 μm pixel pitch, separated by a 300 μm proximity-focusing distance. A monochromator with a spectral resolution of 5 nm was employed to disperse the white light from the CIE standard illuminant A, generating quasi-monochromatic light as the input to the integrating sphere.

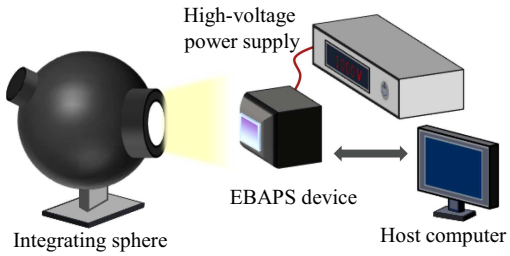


Fig. 3. Schematic of the parameter calibration setup.

For bright-field image acquisition, an optical power meter probe was initially placed at the output port of the integrating sphere to calibrate the optical power density, after which the EBAPS device was positioned at the same location. The device was controlled via a USB interface connected to the host computer, which was used to configure the exposure time and to store the acquired image data. The acceleration voltage was provided by a high-voltage power supply. Dark-field image acquisition followed the same procedure, except that a light-shielding cap was installed on the device and no illumination was applied. Since each parameter demands specific experimental settings (exposure time, acceleration voltage and incident optical power density), six calibration setups (A–F) were configured, as listed in Table 1.

Table 1. Experimental conditions and corresponding calibration parameters.

Group	Calibrated parameter	Symbol	Units	Exposure time (ms)	Acceleration voltage (V)	Incident light ($\mathrm{nw/cm^2}$)
A	photocathode QE	$\eta(\lambda)$	(%)	0 (No driving)	100	wavelength-dependent
B	conversion gain	K	$\mathrm{DN/e^-}$	T_1 [a)]	0	2.5–165
C	pixel dark $\mathrm{e^-}$	$n_{\mathrm{PDe-}}$	$\mathrm{e^-}$/pixel/s	5–40	0	0
D	collection efficiency	CE	%	T_1	300–1200	0.125
E	bias charge	n_{bias}	$\mathrm{e^-}$/pixel	T_1	0	0
	photocathode dark $\mathrm{e^-}$	$n_{\mathrm{DEe-}}$	$\mathrm{e^-}$/pixel/s		1000	
F	shape of read noise	λ_{TL}	Unitless	T_{min} [b)]	0	0
	scale of read noise	σ_{TL}	$\mathrm{e^-}$ rms			

[a)] Default exposure time: 40 ms. [b)] The shortest exposure time: 37 μs.

The QE was calibrated under experimental condition A. This calibration process differs from subsequent parameter calibrations in three aspects. First, the EBAPS device remains powered off. Second, the acceleration voltage is supplied through an electrometer while simultaneously measuring the photocurrent. Third, because the EBAPS device employs a Cs/O-activated GaAs photocathode with a spectral response range of 400–920 nm,[34] the standard monochromatic light

distribution is limited to this wavelength range. At a specific monochromatic wavelength, the QE is defined as the ratio of the number of photoelectrons derived from the measured photocurrent to the number of incident photons calculated from the optical power. The calibration results are presented in Fig. 4. However, the spectral power distribution data of CIE standard illuminant A only covers the 300–830 nm range.[35] To satisfy the requirements of photoelectric conversion modeling, the spectral power distribution $S(\lambda)$ in the 830–920 nm range was extrapolated using Planck's law. This extrapolated segment was then combined with the CIE data in the 300–830 nm range through spectral stitching and unified normalization, yielding a relative spectral power distribution $S'(\lambda)$ spanning 300–920 nm. The photon flux of standard illuminant A was calculated as

$$\phi_{\mathrm{px}} = K_{\mathrm{m}} \int_{380}^{780} S_{560\ \mathrm{nm}} S'(\lambda) V(\lambda) \mathrm{d}\lambda, \tag{13}$$

where $K_{\mathrm{m}} = 683$ lm/W is the maximum luminous efficacy of human vision at 555 nm, and $V(\lambda)$ represents the photopic luminous efficiency function (CIE 1924). Assuming $\phi_{\mathrm{px}} = 1$ lm, the radiant power of standard illuminant A at 560 nm, denoted as $S_{560\ \mathrm{nm}}$, can be computed. Using the relationship $S(\lambda) = S_{560\ \mathrm{nm}} S'(\lambda)$, the spectral power distribution $S(\lambda)$ of illuminant A over the 300–920 nm range can then be derived. The photon distribution $N_{\mathrm{ph}}(\lambda)$ corresponding to a photon flux of 1 lm is given by Eq. (14). The final computed results are presented in Fig. 4.

$$N_{\mathrm{ph}}(\lambda) = \frac{S(\lambda) \cdot \lambda}{hc} \cdot 10^{-9}. \tag{14}$$

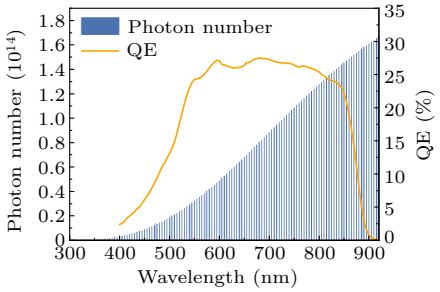


Fig. 4. QE of GaAs photocathode and photon distribution of standard illuminant A (1 lm, 300–920 nm).

The images acquired under experimental condition B were used to calibrate the conversion gain. From this stage onward, all subsequent measurements employed quasi-monochromatic light in the 635–640 nm wavelength range. For each optical power density, the mean gray value μ_y and temporal variance σ_y^2 of multiple image frames captured were calculated, along with the corresponding values for dark-field images ($\mu_{y.\mathrm{dark}}$ and $\sigma^2_{y.\mathrm{dark}}$). A photon transfer curve[36] was plotted using the difference in temporal variance between bright and dark images as the vertical axis, and the difference in mean gray values as the horizontal axis, as shown in Fig. 5(a). A linear fit using the least-squares method yielded a conversion gain K of 2.39 DN/e$^-$.

The pixel dark electrons were calibrated under experimental condition C. Based on the ratio between the average gray level of dark-field images and the conversion gain, the corresponding output charge n_{dark} (units e$^-$/pixel frame) was obtained. Its variation with exposure time is shown in Fig. 5(b). A linear fit using the least-squares method yielded the pixel dark electrons of 32.9 e$^-$/pixel/s.

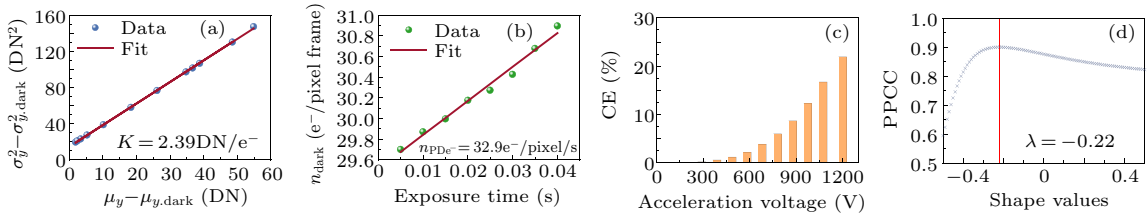


Fig. 5. (a) Estimation of conversion gain. (b) Estimation of pixel dark electrons. (c) Estimation of collection efficiency. (d) Tukey lambda distribution PPCC plot of read noise.

Images obtained under condition D were used to estimate collection efficiency. For a given EBAPS device, only the variation in incident electron energy needs to be considered. For each acceleration voltage, corresponding bright-field and dark-field images were captured. The mean gray value difference in a selected region, denoted as μ_i, was then used to calculate the CE_i as follows:

$$CE_i = \frac{\mu_i}{KG_{\mathrm{EB}}^i (1-\gamma_i) n_{\mathrm{p}} \eta(\lambda)}, \tag{15}$$

where G_{EB}^i and γ_i represent the EBS gain and backscattering coefficient corresponding to the i-th voltage level, respectively. The calibrated results are illustrated in Fig. 5(c).

Under experimental condition E, the bias charge and photocathode dark-emission electrons were calibrated. Mean gray values μ_0 and μ_1 were then calculated from images captured at acceleration voltages of 0 V and 1000 V, respectively. Dividing μ_0 by the conversion gain yields the bias charge of 30.97 e$^-$/pixel. The number of photocathode dark-emission electrons can be obtained from

$$n_{\mathrm{DEe}^-} = \frac{\mu_1 - \mu_0}{KCEG_{\mathrm{EB}}(1-\gamma)T_1}. \tag{16}$$

The result was 0.15 e$^-$/pixel/s.

Here, the values of CE, G_{EB} and γ correspond to the acceleration voltage of 1000 V.

Read noise data were acquired under experimental condition F. After removing the contributions of bias and pixel dark electrons, the shape and scale parameters of read noise were estimated from dark-field image data. As shown in the probability plot correlation coefficient (PPCC) plot in Fig. 5(d), the optimal shape parameter for fitting the data to the Tukey-lambda distribution was determined to be -0.22. The Tukey-lambda distribution is a family of distributions that can approximate many distributions by varying its shape parameter λ_{TL}. When $\lambda_{\mathrm{TL}} = 0.14$, the distribution closely resembles a normal distribution, whereas $\lambda_{\mathrm{TL}} < 0.14$ indicates a heavy-tailed distribution.[14] Since 0.22 is less than 0.14, the data follow a heavy-tailed distribution. Subsequently, the read noise data were fitted using the Tukeylambda distribution probability plot,[38] yielding a scale parameter of 1.69 e^- rms.

4. Experiments and discussion

After acquisition of the parameters for the EBAPS imager used, we verified the established model by comparing simulated and experimental SNRs and limiting resolutions. In contemporary evaluation for night vision devices, SNR and limiting resolution are extensively used as primary indicators for assessing image quality.[39] SNR measures the device's capability in detecting and amplifying low light signals, whereas limiting resolution defines its maximum spatial resolving ability.

4.1. SNR evaluation experiment

A comparative analysis between the simulated and experimental SNR was first performed. The experimental setup was consistent with that shown in Fig. 3, except for three modifications. Specifically, the EBAPS device was equipped with a standard industrial lens with a 50 mm focal length ($f/\# = 0.95$, $\tau = 0.85$), a calibrated 2856 K integrating sphere served as the light source, and its illuminance was measured using a radiometer. During image acquisition, the EBAPS exposure time was set at its default value. Under three low-illumination conditions provided by an integrating sphere light source (2.5×10^{-4} lx, 3.5×10^{-4} lx, and 4.5×10^{-4} lx), images were captured at acceleration voltages ranging from 300 V to 1200 V. For each condition, 50 images were collected. For simulation, a white reference image with an average gray value of 255 was used as the input to represent detection of the integrating sphere light source. To minimize the impact of lens edge distortion, a central region of 60×110 pixels was selected for SNR calculation. For both captured images (with a total of T frames, each of size $M \times N$ pixels) and the corresponding simulated images, the SNR is calculated by

$$\mathrm{SNR} = \frac{\sum_{m=0}^{M-1}\sum_{n=0}^{N-1}\bar{I}[M][N] - \sum_{m=0}^{M-1}\sum_{n=0}^{N-1}\bar{I}_{\mathrm{dark}}[M][N]}{\sum_{m=0}^{M-1}\sum_{n=0}^{N-1}\sqrt{\frac{1}{T-1}\sum_{t=1}^{T}\left(I_t[M][N]-\bar{I}[M][N]\right)^2}}. \tag{17}$$

Here, $I_t[M][N]$ represents the t-th frame bright-field image, $\bar{I}[M][N]$ denotes the corresponding mean gray-level image, and $\bar{I}_{\mathrm{dark}}[M][N]$ represents the average dark image. Figures 6(a)–6(c) plot the SNR versus acceleration voltage for experimental and simulated images at three illumination levels. For each SNR value in Fig. 6, a representative image region is shown, extracted from the central area of the corresponding experimental and simulated video frames at the same acceleration voltage.

These figures show that the SNR trends predicted by the proposed model agree with experimental results across varying acceleration voltages. The SNR remains below 1 between 300 V and 500 V because the EBS gain is too low to suppress read noise and other noise sources. With increasing acceleration voltage, the EBS gain improves and the SNR correspondingly rises. However, this increase does not continue indefinitely. Beyond 900 V, the SNR reaches saturation because the device performance becomes predominantly limited by the photocathode QE. Additionally, at each fixed acceleration voltage, the SNR increases with illumination levels, indicating that the ultimate performance of the device is also constrained by signal-dependent photon shot noise.

Comparisons under three illumination levels reveal certain discrepancies between simulation and experiment. In practice, electron diffusion in the APS degrades the SNR,[40] especially at low acceleration voltages. This effect involves a series of complex lattice-scattering processes, which are not considered in this model, leading to deviations from the experimental results in the 400–800 V range. As the voltage exceeds 800 V, the simulated and experimental SNR curves converge and stabilise. Above 1100 V, however, bright spots appear in the experimental images (green boxes in Fig. 6), which artificially raise pixel gray levels, inducing a sudden increase in the measured SNR. This phenomenon, known as an ion event, occurs when high-energy electrons collide with residual gas molecules in a non-ideal vacuum,[17] and its probability increases with the acceleration voltage. Under 1200 V and higher ambient illumination, a greater number of ion-induced bright spots are observed. Given that the SNR saturates at 1000 V and no significant ion-induced bright spots are visible, 1000 V was adopted as the optimal acceleration voltage for this imager.

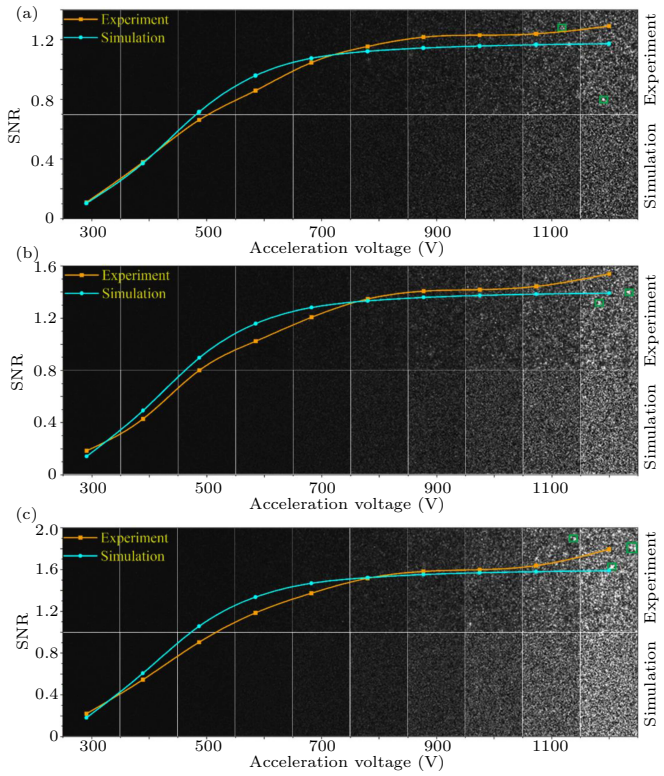


Fig. 6. Comparison of experimental and simulated SNR at varying acceleration voltage levels under different illumination conditions. (a) 2.5×10^{-4} lx. (b) 3.5×10^{-4} lx. (c) 4.5×10^{-4} lx. Ion-induced bright spots are highlighted by green boxes.

At the three illumination levels, the average relative deviations between simulated and measured SNRs were 5.68%, 9.02%, and 8.1%, all below the acceptable 10% threshold, verifying the reliability of the proposed model.

4.2. Limiting resolution evaluation experiment

This section presents a comparative analysis between experimental and simulated results for limiting resolution. The experimental setup is shown in Fig. 7. An integrating sphere provided three low-illumination levels: 5×10^{-5} lx, $1\times10^{-}$ lx, and 2×10^{-4} lx. Under each condition, the EBAPS imager captured images of a negative USAF1951 resolution target positioned 1.5 m away, while operating at the optimal acceleration voltage of 1000 V. The industrial lens and exposure time used were identical to those described in Subsection 4.1. The simulation employed an input image of the negative USAF1951 resolution target, where the grayscale of black and white areas was set to 30 and 240, respectively.

Experimental and simulated images are presented under three illumination levels, as shown in Fig. 8. To facilitate the observation of spatial resolution, the yellow boxed regions in each image were uniformly enhanced using a global linear brightness adjustment. The white scratches appearing in the same locations across all experimental images are device defects. As the ambient illuminance increases, both simulated and experimental images show higher limiting resolution, indicating consistent variation trends. At illumination levels of 5×10^{-5} lx, 1×10^{-4} lx and 2×10^{-4} lx, the measured limiting resolution corresponds to (–4, 4), (–4, 5) and (–2, 1), while the simulated results are (–4, 5), (–4, 6) and (–2, 3), respectively. The simulations are in close agreement with the experiments, with the remaining discrepancies attributable to electron diffusion not being considered in this model. These results confirm the effectiveness of the proposed model for predicting image resolution, while indicating that its accuracy requires further improvement.

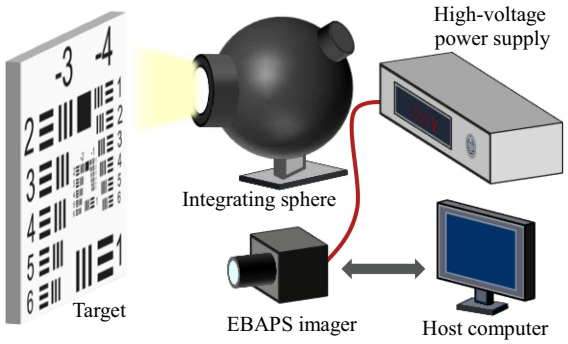


Fig. 7. Schematic of the image acquisition setup.

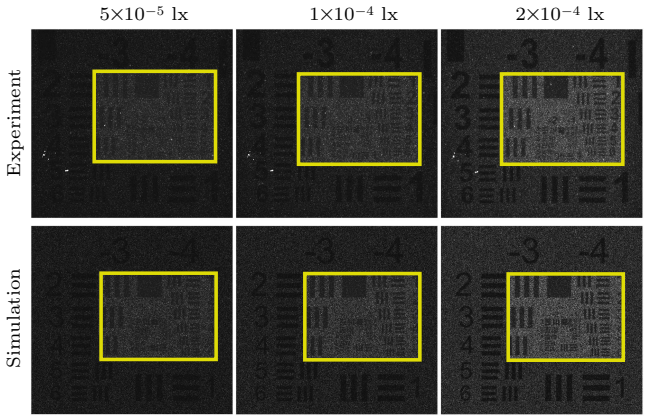


Fig. 8. Comparison of experimental and simulated resolution under different ambient illuminance levels at an acceleration voltage of 1000 V. The yellow boxed regions in each image were processed with a uniform global brightness enhancement to facilitate resolution observation.

5. Effects of key parameters on EBAPS imaging performance

After validating the model, it is used to simulate and analyze the effects of dark noise and proximity distance on the imaging performance of EBAPS. The following simulations are conducted at an illumination level of 2×10^{-4} lx, which was chosen to clearly reveal the variations in SNR and resolution, and at the optimal acceleration voltage of 1000 V. All other parameters and targets are kept consistent with those of the EBAPS imager used in this study.

5.1. Dark noise

The dark noise of the electron-sensitive APS is a key factor limiting SNR at low illumination and the primary motivation for introducing EBS gain. Its variance can be expressed

as

$$\sigma^2_{\text{dark}} = \sigma^2_{\text{TL}} + \sigma^2_{\text{PDe}^-}, \tag{18}$$

where σ^2_{TL} denotes the variance of read noise and $\sigma^2_{\text{PDe}^-}$ represents the variance of pixel dark electrons. In the following analysis, the ratio between these two components is set to be consistent with that of the EBAPS device used in this study. Since the collection efficiency determines the contribution of EBS gain to the signal, SNR curves are plotted against the number of dark noise electrons for different collection efficiencies, as shown in Fig. 9. As dark noise increases, the SNR decreases, with the rate of decline depending on the collection efficiency. When dark noise is below about 2 e^- rms, the differences in decline rates are negligible. Once the dark noise exceeds 5 e^- rms, the SNR curve at 10% collection efficiency drops rapidly, whereas the others remain relatively flat, with the 70% curve showing almost no change. This suggests that the collection efficiency determines the ability of EBS gain to suppress dark noise. A higher collection efficiency makes EBAPS less sensitive to dark noise, thereby reducing its impact on SNR. Thus, under limited operating voltage, improving collection efficiency provides an effective means for EBAPS to mitigate dark noise.

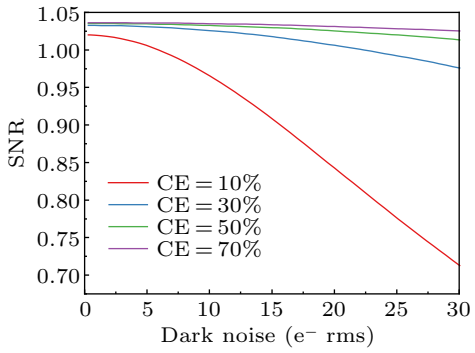


Fig. 9. Variation in SNR with the number of dark noise electrons under different collection efficiencies.

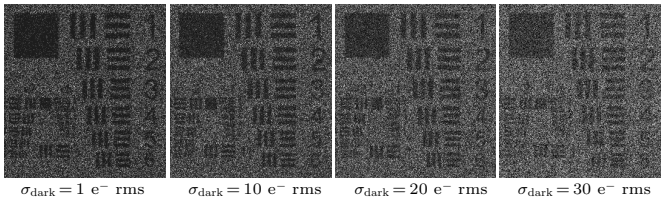


Fig. 10. Image resolution comparison results at different dark noise levels. Each image was uniformly enhanced in brightness to facilitate resolution observation.

Dark noise also constrains image resolution. Cropped regions of the simulated output images under different dark noise levels are shown in Fig. 10. As the noise increases, the background brightness rises, image contrast decreases, and fine details are progressively lost, leading to the degradation of resolution, particularly in groups-2 and -1 (lower-left region of the image). At a dark-noise level of 30 e^- rms, the limiting resolution corresponds to (−2, 2), and the features in group-2 are almost buried by noise. In contrast, at 1 e^- rms, the limiting resolution reaches (−2, 5), where the features remain distinguishable. These results suggest that achieving a lower dark noise level is necessary to observe finer details of the target.

5.2. Proximity-focusing distance

As a structural parameter unique to EBAPS devices, the proximity-focusing distance determines the accuracy of pixel mapping from the photocathode to the APS, thereby affecting the image resolution. Cropped regions of the simulated output images at different proximity distances are shown in Fig. 11. As the distance increases, the image resolution gradually deteriorates. The progressive blurring of the images is manifested by darkening of the gaps between black stripes, merging of adjacent stripes, and the consequent loss of fine details, which is particularly noticeable in elements (−2,1) and (−2, 2) of each image. This effect is different from the loss of details caused by dark noise. A larger proximity-focusing distance enhances the lateral spreading of photoelectrons in the vacuum, thereby reducing the accuracy of pixel mapping from the photocathode to the APS. According to Fig. 11, when the distance is 500 μm, the limiting resolution corresponds to (−2, 2), whereas at 200 μm it reaches (−2, 4). Therefore, shortening the distance can develop the advantage of proximity-focusing configuration and improve the imaging quality of EBAPS imagers.

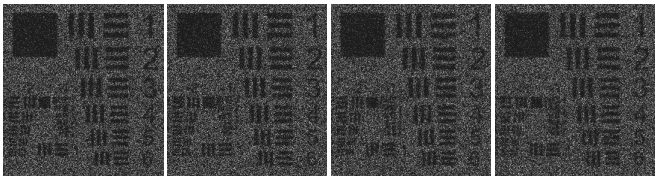


Fig. 11. Image resolution comparison results at different proximity-focusing distances. Each image was uniformly enhanced in brightness to facilitate resolution observation.

6. Conclusion

This study introduces a comprehensive photon-to-gray conversion model for EBAPS imagers, incorporating the full imaging chain. Furthermore, the primary noise sources introduced at each stage of signal transmission are systematically analyzed and characterized. When combined with the proposed parameter-calibration method, the model enables LLL imaging simulations of EBAPS imagers. Validation experiments demonstrate that the relative deviation between simulated and measured SNR values is within 10%. In addition, the simulated and experimental images show comparable limiting resolution with varying illumination levels. These findings verify the effectiveness of the calibration method and the proposed model. Further simulations indicate that higher collection efficiency strengthens the ability of EBS gain to sup-

press dark noise, while a smaller proximity-focusing distance helps preserve fine image details.

Acknowledgement

This work was supported by the National Natural Science Foundation of China (Grant No. U2141239).

References

[1] Sohbati R, Kook M, Jain M, Thomsen K J and Murray A S 2023 *Measurement.* **206** 112234
[2] Raighne A M, Brownlee C, Gebert U, Maneuski D, Milnes J, O'Shea V and Rügheimer T K 2010 *Rev. Sci. Instrum.* **81** 113103
[3] Sobottka S B, Meyer T, Kirsch M, Koch E, Steinmeier R Morgenstern U and Schackert G 2013 *Biomedizinische TechnikBiomedical Engineering* **58** 237
[4] Bai Z, Ma Y, Huang C and Fan X 2019 *3rd International Conference on Electronic Information Technology and Computer Engineering (EITCE)*, October 18–20, 2019, Xiamen, China, p. 1759
[5] Ding D, Shi F and Li Y 2025 *Opt. Laser Technol.* **184** 112553
[6] Nützel G 2011 *Single-Photon Imaging Using Electron Multiplication in Vacuum.* (Berlin: Springer) pp. 73–102
[7] Becker W, Su B, Holub O and Weisshart K 2011 *Microsc. Res. Tech.* **74** 804
[8] Michalet X, Cheng A, Antelman J, Suyama M, Arisaka K and Weiss S 2008 *Proceedings of the Single Molecule Spectroscopy and Imaging*, January 19–24, 2008, San Jose, California, USA, p. 619
[9] Aebi V, Costello K, Yin E, Roderick K, Wilke E, Polukhina L, True B, Bencuya S, Benz R, Huang S, Van Blerkom D, Truong L, Bagwell S, Law W and Lu T 2023 *17th International Image Sensor Workshop*, May 21–25, Scotland, United Kingdom, p. 1
[10] Fossum E R, Teranishi N and Theuwissen A J P 2024 *Annu. Rev. Vis. Sci.* **10** 171
[11] Chao C Y P, Wu T M H, Yeh S F, Lee C L, Tu H, Huang J C Y and Chang C H 2023 *Sensors* **23** 7959
[12] Konnik M and Welsh J 2014 arXiv:1412.4031 [astro-ph.IM]
[13] Zhang Y, Lu X, Wang G, Hu Y and Xu J 2016 *Chin. Phys. B* **25** 070503
[14] Wei K, Fu Y, Zheng Y and Yang J 2021 *IEEE Trans. Pattern Anal. Mach. Intell.* **44** 8520
[15] Bu F, Yao D, Yang Y and Cao W 2023 *Third International Conference on Optics and Image Processing*, April 14–16, 2023, Hangzhou, China, p. 121
[16] Rabner A and Shacham-Diamand Y 2011 *IEEE Sens. J.* **11** 186
[17] Hirvonen L M and Suhling K 2016 *Sensors.* **16** 617
[18] Wang W, Li Y, Chen W, Song D and Wang X 2020 *IEEE Photon. J.* **12** 6901210
[19] Wang X, Song D, Jiao G, Li Y and Chen W 2022 *IEEE Photon. J.* **14** 6858605
[20] Chen W, Chen W, Song D, Zhao P, Li Y, Li S, Wang C, Liang R and Yue J 2024 *Nucl. Instrum. Methods Phys. Res., Sect. B* **551** 165352
[21] Faiz W, Li J, Gao K, Wu Z, Lei Y H, Huang J H and Zhu P P 2020 *Chin. Phys. B* **29** 014301
[22] Bai J, Bai Y, Hou X, Cao W, Yang Y, Wang B, Bai X and Li S 2020 *Mod. Phys. Lett. B* **34** 2050398
[23] Dietz K 2010 *Standards and procedures for application of radiometric sensors* (White Sands Missile Range, NM: Range Commanders Council) pp. 179–180
[24] Benjamin J R and Cornell C A 2014 *Probability, statistics, and decision for civil engineers* (Courier Corporation) p. 151
[25] Gow R D, Renshaw D, Findlater K, Grant L, McLeod S J, Hart J and Nicol R L 2007 *IEEE Trans. Electron Devices.* **54** 1321
[26] Ren L, Shi F, Guo H, Wang H and Chang B 2013 *Appl. Opt.* **52** 1641
[27] Stearns D and Wiedwald J 1989 *Rev. Sci. Instrum.* **60** 1095
[28] Hirvonen L M, Jiggins S, Sergent N, Zanda G and Suhling K 2014 *Rev. Sci. Instrum.* **85** 95
[29] Joy D C 1995 *Scanning.* **17** 270
[30] Suyama M, Fukasawa A, Haba J, Iijima T, Iwata S, Sakuda M, Sumiyoshi T, Takasaki F, Tanaka M, Tsuboyama T and Yamada Y 2004 *Nucl. Instrum. Methods Phys. Res. A* **523** 147
[31] Kotov I V, Neal H, O'Connor P 2018 *Nucl. Instrum. Methods Phys. Res., Sect. A* **901** 126
[32] Rodrigues D, Andersson K, Cababie M, Donadon A, Botti A, Cancelo G, Estrada J, Fernandez-Moroni G, Piegaia R and Senger M 2021 *Nucl. Instrum. Methods Phys. Res., Sect. A* **1010** 165511
[33] Aebi V and Costello K 2011 *Single-Photon Imaging* (Berlin: Springer) pp. 63–72
[34] Fang C, Zhang Y, Zhang K, Shi F, Jiao G, Cheng H, Dai Q and Zhang J 2019 *Appl. Opt.* **58** 5281
[35] CIE standard illuminant A–1 nm
[36] Stefanov K D, Clarke A S, Ivory J and Holland 2018 *Sensors.* **18** 118
[37] Freimer M, Kollia G, Mudholkar G S and Thomas Lin C 1989 *Communications in Statistics-Theory and Methods.* **18** 4261
[38] Wilk M B and Gnanadesikan R 1968 *Biometrika* **55** 1
[39] FOM in Night Vision Devices
[40] Ahn J, Lee K, Kim Y, Jeong H, Kim B and Kim H 2014 *Proc. IEEE International Conference on Solid-State Circuits (ISSCC),* Februrary 9–13, 2014, San Francisco, USA, p. 124